ChemComm

COMMUNICATION

View Article Online
View Journal | View Issue

Cite this: *Chem. Commun.*, 2024, **60**, 9938

Received 13th July 2024,
Accepted 12th August 2024

DOI: 10.1039/d4cc03501a

rsc.li/chemcomm

Long-wavelength triggered iridium(III) complex nanoparticles for photodynamic therapy against hypoxic cancer†

Shengnan Liu,[a] Ziwei Wang,[a] Zihan Wu,[a] Haoran Chen,[b] Dongxia Zhu,*[a] Gungzhe Li,*[c] Mingming Yan,[c] Martin R. Bryce*[d] and Yulei Chang*[b]

A long-wavelength triggered cationic iridium(III) complex, Ir5, and its corresponding nanoparticles with the ability to generate type I and type II reactive oxygen species have been synthesised. The complex targets mitochondria and achieves an excellent photodynamic therapy effect in hypoxic cancer cells.

The significant cytotoxicity of reactive oxygen species (ROS) and the precision of light-irradiation make photodynamic therapy (PDT) advantageous for broad-spectrum anticancer activity.[1–3] However, clinical applications of conventional high-O_2-dependent PDT processes are hindered by the hypoxic tumor microenvironment (TME) with insufficient oxygen supply.[4,5] Many efforts have been made to enhance the concentration of O_2 in tumors, such as exogenous O_2 delivery and catalysis of H_2O_2 to generate O_2, *etc.*, but they face complex materials designs.[6,7] Currently, type I photosensitizers (PSs) have great potential to alleviate the adverse effect of hypoxia on PDT.

Cyclometalated Ir(III) complexes with high intersystem crossing (ISC) ability induced by the heavy atom effect, high photo- and thermal-stability, and tunable optical and excited state behaviour are promising PSs that enhance ROS production for PDT.[8–11] Meanwhile, the rich photo-physicochemical properties of Ir(III) complexes derived from various electronic excited-states obtained upon irradiation facilitate electron-transfer processes that allow type I ROS generation photoreaction pathways.[11–13] However, the irradiation source of traditional Ir complex PSs is mainly in the blue and UV regions, which seriously limits the light penetration depth and thus obstructs the efficacy of the PSs to generate ROS in many affected areas.[14–16] Therefore, the development of long-wavelength irradiated Ir complexes as PSs is an urgent problem.

High ROS generation efficiency of PSs with absorption in long-wavelength regions can be achieved *via* a self-assembly-induced vibronic decoupling strategy.[17] A rigid molecular structure can reduce the equilibrium displacement between ground and excited states and reduce structural distortion; however, such structures often suffer from poor solubility and difficulty in synthesis.[17] At present, there are only a few reports on long-wavelength excited Ir complexes as PSs, especially for type I ROS production, which still remain to be developed.[17,18]

Herein, we designed a long-wavelength activated Ir complex, **Ir5**, by introducing extended π-conjugated C^N ligands combined with a functionalised Schiff base as auxiliary N^N ligand to produce type I and type II ROS (Scheme 1). **Ir5 NPs** were constructed, and they demonstrate much higher phototoxicity than conventional PSs [rhodamine-B (RB), chlorin e6 (Ce6), zinc phthalocyanine (ZnPc) and hematoporphyrin (HpD)] upon 655 nm irradiation in hypoxic cells due to the **Ir5 NPs**' outstanding ability to produce type I ROS, implying their potential for hypoxic PDT applications. Moreover, **Ir5 NPs** localize in mitochondria after 6 h in 4T1 cells and induce cell apoptosis. Our work establishes a new platform for the design, synthesis and application of long-wavelength triggered metal complex PSs in hypoxic PDT (Scheme 1).

Five Ir complexes of general structure $[Ir(C^N)_2(N^N)]^+ PF_6^-$ were synthesized by using a functionalised Schiff base N^N ligand and C^N ligands with different degrees of π-conjugation, sequentially named **Ir1–Ir5**, as the conjugation increased. Their structures are shown in Scheme S5 (ESI†) and the synthetic routes are shown in Schemes S1–S5 (ESI†). The molecular structures were validated by nuclear magnetic resonance (^1H NMR and ^{13}C NMR) spectroscopy, mass spectrometry (Fig. S1–S18, ESI†) and elemental analysis.

[a] *Key Laboratory of Nanobiosensing and Nanobioanalysis at Universities of Jilin Province, Department of Chemistry, Northeast Normal University, 5268 Renmin Street, Changchun, Jilin Province 130024, P. R. China. E-mail: zhudx047@nenu.edu.cn*

[b] *State Key Laboratory of Luminescence and Applications, Changchun Institute of Optics, Fine Mechanics and Physics, Chinese Academy of Sciences, Changchun, Jilin Province 130033, China. E-mail: yuleichang@ciomp.ac.cn*

[c] *Jilin Provincial Science and Technology Innovation Center of Health Food of Chinese Medicine, Changchun University of Chinese Medicine, Changchun, Jilin Province 130117, P. R. China. E-mail: 1993008106@qq.com*

[d] *Department of Chemistry, Durham University, Durham, DH1 3LE, UK. E-mail: m.r.bryce@durham.ac.uk*

† Electronic supplementary information (ESI) available: Experimental details, supporting figures and tables. See DOI: https://doi.org/10.1039/d4cc03501a

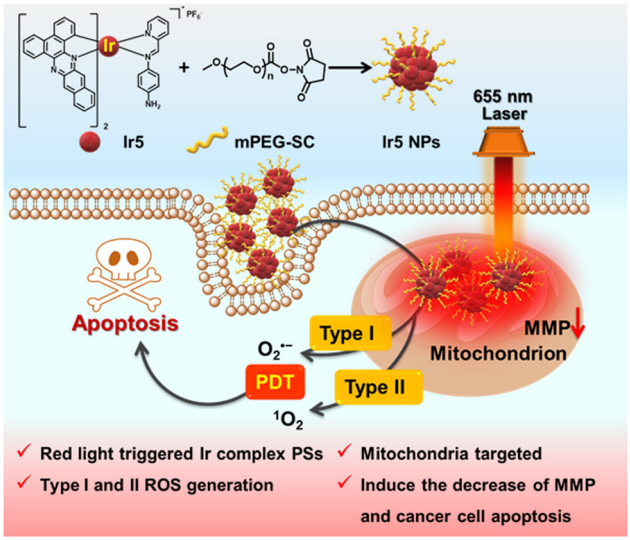

Scheme 1 Schematic diagram of **Ir5** structure and long-wavelength triggered PDT using **Ir5 NPs**.

The photophysical properties of **Ir1–Ir5** are shown in Fig. 1a, b, Fig. S19, S20 and Table S1 (ESI†). **Ir1–Ir5** exhibit strong absorption at 250–350 nm mainly due to π–π* transitions at the ligand center. The absorption of **Ir1**, **Ir2**, and **Ir3** is mainly in the blue region; with increasing conjugation of the C^N ligands the absorption of **Ir4** and **Ir5** gradually red-shifts, and the relative intensity in the green and red regions increases. Notably, **Ir5** still absorbs at around 655 nm (ε = 1000 L M^{-1} cm^{-1}) with the tail extending to 700 nm (Fig. 1b and Fig. S21, ESI†), which allows its application for red-light triggered PSs in PDT. Meanwhile, the emission peaks of **Ir1–Ir5** gradually red-shift with increasing π-conjugation (Fig. S20, ESI†) as designed.[19,20] As shown in Fig. S22 (ESI†), no significant change in the absorption spectra of **Ir1–Ir5** within 30 min of irradiation imply their excellent photostability, which is a prerequisite for the application of PSs in PDT.[21,22]

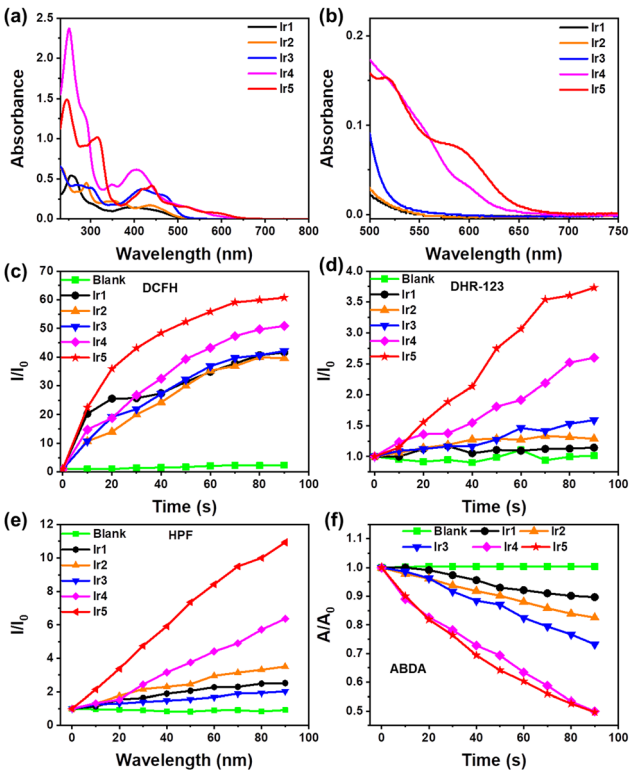

Fig. 1 (a) The UV-vis absorption spectra of **Ir1–Ir5** in CH_3CN : H_2O (1 : 90 v/v). (b) The enlarged spectra (500–750 nm) of (a). The change of PL intensity of DCFH (c), DHR 123 (d) and HPF (e) with the change of time in different solutions. (f) The decay rates of ABDA in different solutions.

To further investigate the PDT potential of **Ir1–Ir5**, 2,7-dichlorodihydrofluorescein (DCFH) was used as a luminescent indicator to detect their ROS generation ability. As shown in Fig. 1c and Fig. S23 (ESI†), there is almost no difference in the ROS production from **Ir1–Ir3** under 90 s of irradiation, whereas **Ir4** and **Ir5** have stronger ROS production capacity. In particular, the DCFH in **Ir5** solution emits brighter at 525 nm within 90 s of light exposure (about 60 times of I_0), indicating that **Ir5** has the highest ROS generation ability in the series. Subsequently, the type of ROS produced by **Ir1–Ir5** was established. Dihydrorhodamine 123 (DHR 123) was used as a type I ROS indicator to detect the $O_2^{\bullet-}$ generation from **Ir1–Ir5**. Similar to the above trend of the total ROS production, **Ir1–Ir3** produce only minor $O_2^{\bullet-}$, while **Ir5** exhibits excellent $O_2^{\bullet-}$ generation ability ≈3 times of **Ir1–Ir3** (Fig. 1d and Fig. S24, ESI†). These results are supported by electron paramagnetic resonance (EPR) spectroscopy using 2,2-dimethyl-1-oxido-3,4-dihydropyrrol-1-ium (DMPO) as a scavenger of $O_2^{\bullet-}$ (Fig. S27a, ESI†), in which **Ir5** shows the strongest spin signal in the series. Furthermore, the outstanding $^{\bullet}OH$ generation ability of **Ir5** was detected by hydroxyphenyl fluorescein (HPF) (Fig. 1e and Fig. S25, ESI†), suggesting the potential of **Ir5** for PDT against hypoxic cancer. Moreover, 2-[10-(2,2-dicarboxyethyl)anthracen-9-yl]methylpropanedioic acid (ABDA) was used as an indicator of $^1O_2$ to assess type II ROS production upon irradiation. The ability of **Ir1–Ir3** to produce $^1O_2$ gradually increases, **Ir1** < **1r2** < **1r3**, but the absorption of ABDA remains >70% of A_0 after 90 seconds of light exposure, while **Ir4** and **Ir5** produce $^1O_2$ more efficiently with A/A_0 < 50% after 90 s (Fig. 1f and Fig. S26, ESI†). These results are consistent with the EPR results using 2,2,6,6-tetramethyl-4-piperidone hydrochloride (TEMP) to scavenge $^1O_2$ (Fig. S27b, ESI†). An enhanced spin signal was observed for **Ir4** and **Ir5**, indicating increased $^1O_2$ production. The above results demonstrate that the Ir complexes generate both type I and type II ROS, with potential applications as PSs for PDT. Therefore, **Ir5** with the highest ROS production ability was used to construct nanoparticles (NPs) for subsequent *in vitro* cell studies.

Ir5 NPs were constructed by linking the –NH_2 on the N^N ligand of **Ir5** with PEG containing an activated succinimidyl ester unit (PEG-Sc) (Scheme 1).[23] The FT-IR spectra showed that the peak at 3384 cm^{-1} for –NH_2 in **Ir5** disappeared in **Ir5 NPs** and the peak of active ester in PEG-Sc at 1800–1730 cm^{-1} disappeared in **Ir5 NPs** indicating the successful conjugation of **Ir5** and PEG in **Ir5 NPs** (Fig. S28, ESI†). Compared with **Ir5**, there is a red-shift in the absorption spectrum of **Ir5 NPs** (Fig. 2a). **Ir5 NPs** emit at 875 nm, which corresponds to the emission of **Ir5** (Fig. S29, ESI†). Meanwhile, the fluid dynamic

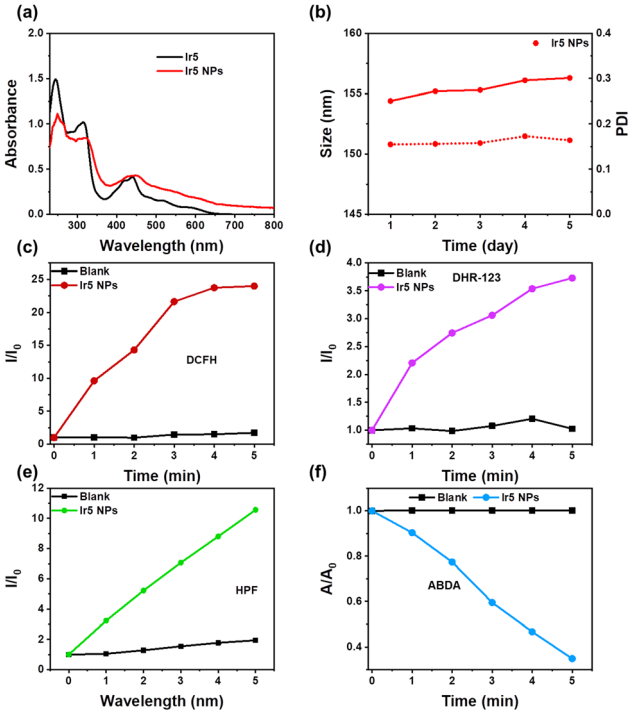

Fig. 2 (a) The UV-vis absorption spectra of **Ir5** and **Ir5 NPs**. (b) The DLS data for **Ir5 NPs** during 6 days. Solid line: size. Dashed line: PDI. The change of PL intensity of DCFH (c) DHR 123 (d) and HPF (e) with the change of time in **Ir5 NPs** solutions. (f) The decay rates of ABDA in **Ir5 NPs** solutions.

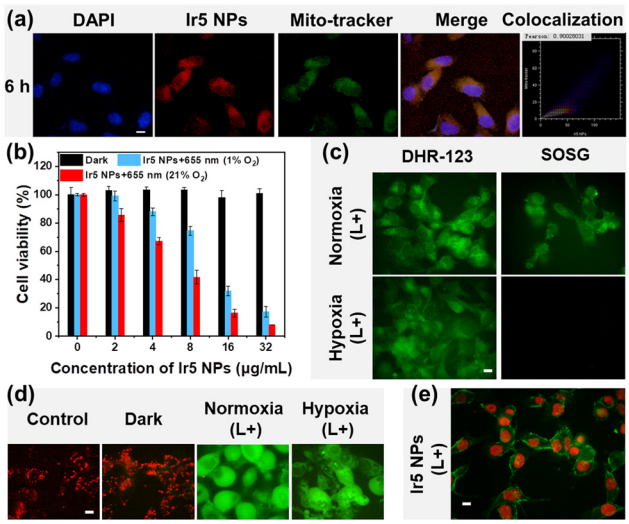

Fig. 3 (a) CLSM images of 4T1 cells after incubation with **Ir5 NPs** and colocalization assay of **Ir5 NPs** with MitoTracker Green. (b) Relative viability of 4T1 cells after co-incubation with **Ir5 NPs** under different conditions. Confocal fluorescence images for the detection of ROS generation (c), the detection of MMP *via* JC-1 dye assay (d) and cell death detection by dual fluorescence of Annexin V-FITC/PI staining (e) in 4T1 cells treated with **Ir5 NPs** under different conditions. Scale bar = 10 μm.

size of **Ir5 NPs** measured by dynamic light scattering (DLS) was 154.4 nm, and the polydispersity index (PDI) was 0.155 (Fig. S31, ESI†). Within 5 days, there was no significant change in the particle size and PDI of **Ir5 NPs** (Fig. 2b), indicating their good stability in phosphate-buffered saline (PBS) for subsequent PDT research.

The ROS production ability of **Ir5 NPs** was tested under 655 nm laser irradiation (Fig. 2c–f and Fig. S32–S35, ESI†). Compared with the blank control group, with the increase of illumination time, the fluorescence intensity of DCFH, DHR-123 and HPF is significantly enhanced, and the absorbance of ABDA degraded to below 40% within 5 minutes. These results indicate that **Ir5 NPs** can produce type I and type II synergistic ROS under 655 nm laser irradiation, which suggests their suitability for PDT of hypoxic cancer cells *in vitro*.

The *in vitro* cell experiments of **Ir5 NPs** were conducted using mouse breast cancer cells (4T1 cells) as a readily available model cell line. The uptake of **Ir5 NPs** in 4T1 cells was investigated through confocal laser scanning microscopy (CLSM) and the subcellular distributions of **Ir5 NPs** were studied by co-staining experiments with MitoTracker Green (Fig. 3a and Fig. S36, ESI†). After incubation time of 1 h, the luminescence of **Ir5 NPs** was almost invisible; at 3 h the **Ir5 NPs** gradually accumulated in the cells and when the incubation time reached 6 h, the luminescence in 4T1 cells was brighter, indicating a significant increase of the **Ir5 NPs** content. The excellent overlap between the luminescence of Mito-Tracker Green and the **Ir5 NPs** gave a high Pearson's correlation coefficient (PCC) of above 0.90, revealing selective accumulation of **Ir5 NPs** in mitochondria. Mitochondria are ideal organelles for PDT as the accumulation of ROS decreases the mitochondrial membrane potential (MMP), ultimately leading to cell death.[24,25]

MTT assay was conducted to verify the PDT effect of **Ir5 NPs** (Fig. 3b) (MTT = [3-(4,5-dimethylthiazol-2-yl)-2,5-diphenyltetrazolium bromide]). The viability of 4T1 cells was evaluated under various conditions *in vitro*. Under darkness, **Ir5 NPs** showed no significant toxicity to 4T1 cells, while under laser irradiation at 655 nm (150 mW cm^{-2}), **Ir5 NPs** exhibited high phototoxicity with an IC_{50} value of 6.43 μg mL^{-1}. Moreover, **Ir5 NPs** still exhibit good phototoxicity to 4T1 cells under hypoxic conditions, with an IC_{50} value of 11.71 μg mL^{-1}. Further MTT assays were carried out to compare the cytotoxic effects of conventional PSs (RB, Ce6, ZnPc and HpD) and **Ir5 NPs** (Fig. S37 and Table S2, ESI†). Although Ce6, ZnPc and HpD show outstanding phototoxicity similar to **Ir5 NPs** at normoxic conditions, there are almost no change of 4T1 cells' viability at hypoxic conditions upon irradiation (Table S2, ESI†). The obvious contrast is mainly because these conventional type II PSs have high oxygen dependency during PDT, while **Ir5 NPs** can still produce cytotoxic type I ROS to induce cell death under hypoxic conditions. The live–dead cell staining experiments further tested the cytotoxicity of **Ir5 NPs** (Fig. S38, ESI†). The hypoxic cells incubated with **Ir5 NPs** still have red fluorescence after irradiation, suggesting the cell phototoxicity of **Ir5 NPs**, consistent with the MTT assay results. The above results indicate that **Ir5 NPs** exhibit excellent phototoxicity to cancer cells under irradiation. Compared with conventional PSs, **Ir5 NPs** exhibit better phototoxicity in hypoxic cells. This demonstrates the potential of **Ir5 NPs** for long-wavelength-triggered PDT for hypoxic cancer cells.

The intracellular photoinduced ROS generation ability of **Ir5 NPs** was investigated in 4T1 cells (Fig. 3c and Fig. S39, ESI†). The total ROS level of cells treated with **Ir5 NPs** was monitored with DCFH-DA as a probe. Confocal imaging revealed negligible green fluorescence in the control and dark groups (L−), while obvious green fluorescence was observed after 655 nm irradiation (L+), proving the excellent ROS generation ability of **Ir5 NPs**. To better understand the mechanism of ROS generation, the ability of **Ir5 NPs** to produce type II and type I ROS was tested separately by singlet oxygen sensor green (SOSG) and DHR-123. Compared with the control group and the dark groups, the irradiated group shows green fluorescence of DHR-123 under both normoxic and hypoxic conditions, indicating **Ir5 NPs** undergo effective type I photochemical process under irradiation. In contrast, there is almost no SOSG signal in the groups under hypoxic conditions because the low-O_2 concentration limits the type II process to produce $^1O_2$. It is therefore clear that **Ir5 NPs** have excellent capacity to produce both type I and type II ROS, and mainly undergo type I PDT processes under hypoxic conditions.

To further investigate the mechanism of PDT-induced 4T1 cell death using **Ir5 NPs**, changes in MMP were detected by JC-1 dye (a cationic carbocyanine derivative) (Fig. 3d and Fig. S40, ESI†). The red fluorescence of aggregated JC-1 was observed in the control and dark groups. However, after irradiation, there was green fluorescence of monomer JC-1 in the cytoplasm, indicating a decrease of MMP. MMP is important for maintaining cell operation, as well as a key factor affecting cell apoptosis.[24] Furthermore, dual fluorescence staining with Annexin V-FITC/PI (propidium iodide) characterized the cell apoptosis induced by PDT. As shown in Fig. 3e and Fig. S41 (ESI†), after irradiation, the 4T1 cells treated with **Ir5 NPs** exhibited significant green fluorescence, and their nuclei were stained with PI, indicating the occurrence of early apoptosis. The above results verify that apoptosis is the cell death mechanism during PDT using **Ir5 NPs** PDT.

In summary, a long-wavelength triggered Ir(III) complex was successfully designed and synthesized by extending the π-conjugation of the C^N ligands and using a modifiable and functional Schiff base N^N ligand. **Ir5 NPs** with excellent stability were constructed through condensation with PEG-Sc; the NPs induce outstanding type I and II ROS generation upon 655 nm laser irradiation. *In vitro* experiments demonstrate that **Ir5 NPs** are taken up by 4T1 cells and target mitochondria. Comparing with the classic PSs (RB, Ce6, ZnPc and HpD), **Ir5 NPs** exhibit better phototoxicity under hypoxic conditions due to the excellent ability to produce type I and II ROS in hypoxic cells. The irradiated-**Ir5 NPs** decrease the MMP and induce cell apoptosis. This work will provide a valuable benchmark for the future design of metal complex PSs with long-wavelength absorption and type 1 PDT applications.

This work was funded by NSFC (no. 52073045, 62075217, 62305329), Science and Technology Development Plan Project of Jilin Province (20240402036GH, 20210101148JC, 20230508104RC, DZJ202301ZYTS114), the Development and Reform Commission of Jilin Province (2020C035-5, 2023C029-2), China Postdoctoral Science Foundation (2023M733432) and Chunhui project (HZKY20220377). M. R. B. thanks EPSRC (UK) grant EP/L02621X/1 for funding.

Data availability

The data associated with this article is available in the manuscript and ESI.†

Conflicts of interest

There are no conflicts to declare.

Notes and references

1 D. Mitton and R. Ackroyd, *Photodiagn. Photodyn. Ther.*, 2008, **5**, 103–111.
2 Z. Zhou, J. Song, L. Nie and X. Chen, *Chem. Soc. Rev.*, 2016, **45**, 6597–6626.
3 X. Zhong, X. Wang, J. Li, J. Hu, L. Cheng and X. Yang, *Coord. Chem. Rev.*, 2021, **437**, 213828.
4 D. M. Brizel, S. Lin, J. L. Johnson, J. Brooks, M. W. Dewhirst and C. A. Piantadosi, *Br. J. Cancer*, 1995, **72**, 1120–1124.
5 A. L. Gill and C. N. A. Bell, *QJM*, 2004, **97**, 385–395.
6 A. Sahu, I. Kwon and G. Tae, *Biomaterials*, 2020, **228**, 119578.
7 C. Zhang, X. Hu, L. Jin, L. Lin, H. Lin, Z. Yang and W. Huang, *Adv. Healthcare Mater.*, 2023, e2300530.
8 S. Liu, J. Han, Y. Chang, W. Wang, R. Wang, Z. Wang, G. Li, D. Zhu and M. R. Bryce, *Chem. Commun.*, 2022, **58**, 10056–10059.
9 S. Liu, J. Han, W. Wang, Y. Chang, R. Wang, Z. Wang, G. Li, D. Zhu and M. R. Bryce, *Dalton Trans.*, 2022, **51**, 16119–16125.
10 Y. Pei, J. Xie, D. Cui, S. Liu, G. Li, D. Zhu and Z. Su, *Dalton Trans.*, 2020, **49**, 13066–13071.
11 D. Chen, Q. Xu, W. Wang, J. Shao, W. Huang and X. Dong, *Small*, 2021, **17**, e2006742.
12 S. Liu, Y. Pei, Y. Sun, Z. Wang, H. Chen, D. Zhu, M. R. Bryce, B. Z. Tang and Y. Chang, *Aggregate*, 2024, e547.
13 F. Wei, J. Karges, J. Shen, L. Xie, K. Xiong, X. Zhang, L. Ji and H. Chao, *Nano Today*, 2022, **44**, 101509.
14 J. Zhao, X. Zhang, L. Fang, C. Gao, C. Xu and S. Gou, *Small*, 2020, **16**, e2000363.
15 D. B. L. Teh, A. Bansal, C. Chai, T. B. Toh, R. A. J. Tucker, G. G. L. Gammad, Y. Yeo, Z. Lei, X. Zheng, F. Yang, J. S. Ho, N. Bolem, B. C. Wu, M. K. Gnanasammandhan, L. Hooi, G. S. Dawe, C. Libedinsky, W. Y. Ong, B. Halliwell, E. K. Chow, K. L. Lim, Y. Zhang and B. K. Kennedy, *Adv. Mater.*, 2020, **32**, e2001459.
16 A. W. Sainter, T. A. King and M. R. Dickinson, *J. Biomed. Opt.*, 2004, **9**, 193–199.
17 J. Zhao, Y. Gao, R. Huang, C. Chi, Y. Sun, G. Xu, X. H. Xia and S. Gou, *J. Am. Chem. Soc.*, 2023, **145**, 11633–11642.
18 J. Zhao, K. Yan, G. Xu, X. Liu, Q. Zhao, C. Xu and S. Gou, *Adv. Funct. Mater.*, 2021, **31**, 2008325.
19 Y. Li, N. Dandu, R. Liu, Z. Li, S. Kilina and W. Sun, *J. Phys. Chem. C*, 2014, **118**, 6372–6384.
20 A. F. Henwood, D. Antón-García, M. Morin, D. R. Martir, D. B. Cordes, C. Casey, A. M. Z. Slawin, T. Lebl, M. Bühl and E. Zysman-Colman, *Dalton Trans.*, 2019, **48**, 9639–9653.
21 Y. Chen, L. Qiao, L. Ji and H. Chao, *Biomaterials*, 2014, **35**, 2–13.
22 C. W. T. Leung, Y. Hong, S. Chen, E. Zhao, J. W. Y. Lam and B. Z. Tang, *J. Am. Chem. Soc.*, 2013, **135**, 62–65.
23 S. Lee, S. Kim, J. Choo, S. Y. Shin, Y. H. Lee, H. Y. Choi, S. Ha, K. Kang and C. H. Oh, *Anal. Chem.*, 2007, **79**, 916–922.
24 S. Kuang, F. Wei, J. Karges, L. Ke, K. Xiong, X. Liao, G. Gasser, L. Ji and H. Chao, *J. Am. Chem. Soc.*, 2022, **144**, 4091–4101.
25 R. Wang, X. Li and J. Yoon, *ACS Appl. Mater. Interfaces*, 2021, **13**, 19543–19571.